scientific reports

Check for updates

OPEN

Hemodynamic effects of entry and exit tear size in aortic dissection evaluated with in vitro magnetic resonance imaging and fluid–structure interaction simulation

Judith Zimmermann[1,5], Kathrin Bäumler[1,5✉], Michael Loecher[1,4], Tyler E. Cork[1,2], Alison L. Marsden[2,3], Daniel B. Ennis[1,4] & Dominik Fleischmann[1]

Understanding the complex interplay between morphologic and hemodynamic features in aortic dissection is critical for risk stratification and for the development of individualized therapy. This work evaluates the effects of entry and exit tear size on the hemodynamics in type B aortic dissection by comparing fluid–structure interaction (FSI) simulations with in vitro 4D-flow magnetic resonance imaging (MRI). A baseline patient-specific 3D-printed model and two variants with modified tear size (smaller entry tear, smaller exit tear) were embedded into a flow- and pressure-controlled setup to perform MRI as well as 12-point catheter-based pressure measurements. The same models defined the wall and fluid domains for FSI simulations, for which boundary conditions were matched with measured data. Results showed exceptionally well matched complex flow patterns between 4D-flow MRI and FSI simulations. Compared to the baseline model, false lumen flow volume decreased with either a smaller entry tear (– 17.8 and – 18.5%, for FSI simulation and 4D-flow MRI, respectively) or smaller exit tear (– 16.0 and – 17.3%). True to false lumen pressure difference (initially 11.0 and 7.9 mmHg, for FSI simulation and catheter-based pressure measurements, respectively) increased with a smaller entry tear (28.9 and 14.6 mmHg), and became negative with a smaller exit tear (– 20.6 and – 13.2 mmHg). This work establishes quantitative and qualitative effects of entry or exit tear size on hemodynamics in aortic dissection, with particularly notable impact observed on FL pressurization. FSI simulations demonstrate acceptable qualitative and quantitative agreement with flow imaging, supporting its deployment in clinical studies.

Aortic dissection is a life-threatening cardiovascular disease, typically presenting with an acute and dramatic onset, followed by a chronic life-long phase of increased risk for late adverse events. An estimate of up to 138,000 individuals in the United States alone live with chronic aortic dissection[1]. Its pathological substrate and hallmark is the formation of a secondary flow channel within the aorta, the false lumen (FL), caused by abrupt delamination of the inner aortic wall layers. The delaminated tissue that seperates the FL from the original true lumen (TL) is referred to as the dissection flap. Blood flow enters the FL through the entry tear upstream, and returns to the TL downstream through one or more exit tears[2]. The outer boundary of the FL is mechanically weak and prone to fatal aortic rupture, particularly in the first 24 to 48 h[3], which presents the most common cause of death in the acute phase. Other major concerns are branch vessel ischemia resulting in organ malperfusion, and aneurysmal dilation of the FL. For all patients reaching the chronic phase, life-long clinical monitoring is mandatory, and surgical or endovascular intervention is required in 40 to 60% of patients within the first 5 years[4,5].

[1]Department of Radiology, Stanford University, Stanford, CA, USA. [2]Department of Bioengineering, Stanford University, Stanford, CA, USA. [3]Department of Pediatrics, Stanford University, Stanford, CA, USA. [4]Division of Radiology, Veterans Affairs Health Care System, Palo Alto, CA, USA. [5]These authors contributed equally: Judith Zimmermann and Kathrin Bäumler. ✉email: baeumler@stanford.edu

Anatomical characteristics of aortic dissections vary substantially between patients. Specifically, an aortic dissection without the involvement of the ascending aorta (Stanford type B aortic dissection, TBAD) is managed medically for the majority of patients (60 to 70%)[1]. However, studies suggest that late adverse events occur in 34 to 38% of initially uncomplicated TBADs[1]. According to latest guidelines[6], preventive thoracic endovascular aortic repair (TEVAR) may be considered for TBAD; nevertheless, the role and timing of TEVAR remains an evolving matter of debate.

Surveillance imaging is critical to identify potentially vulnerable patients and initiate intervention informed by measurable predictive biomarkers. A number of previous works investigated morphological features that were mostly derived from computed tomography angiography (CTA) image data[7–14]. Adding to morphological measures, recent studies increasingly investigated hemodynamics to further advance prediction models. For example, decreased outflow through FL branch vessels[11], increased FL ejection fraction[15–17], and FL pressurization[18–20] were determined to promote late adverse events. Further, these hemodynamic features have been associated with patient-specific morphology. Cuellar-Calabria et al.[21] presented entry tear dominance (i.e. entry tear much larger than exit tear) as a multivariable predictor, while Fleischmann and Burris[22] hypothesize a linkage between tear dominance, increased outflow resistance, and resulting FL pressurization. That is, to optimize risk stratification, predictive models must comprise both morphological and hemodynamic indices.

Hemodynamic parameters can be obtained via computational fluid dynamics (CFD) and through flow imaging. CFD simulates patient-specific flow fields and pressures at high spatio-temporal resolution, and fluid–structure interaction (FSI) additionally incorporates the effects of the deformable vessel wall[23,24]. If simulations were able to reliably replicate in vivo hemodynamics, it would tremendously expand non-invasive means to predict risk related to pathological changes and response to interventions. Numerous studies have deployed CFD frameworks (with and without FSI) to study hemodynamics in patient-specific TBAD geometries[18–20,25–27]. But, all face three key technical challenges: (1) it is difficult to obtain accurate patient-specific material parameters such as wall stiffness and fluid viscosity; (2) sparse clinical data, particularly of luminal pressure, often prevents a complete prescription of the boundary conditions; and (3) lacking in vivo measured flow and pressure data hinders rigorous validation.

4D-flow magnetic resonance imaging (MRI) measures time-resolved 3D vector-valued velocity maps within a 3D volume of interest[28], and has shown promising potential for measuring flow dynamics in dissections[29–31]. Owing to lengthy scan times, however, clinical in vivo 4D-flow MRI must be performed using high acceleration rates and ultra-fast sequences, but trades-off in spatio-temporal image resolution and signal-to-noise-ratio (SNR) are inevetiable[32–37]. Sub-optimal data quality ultimately hampers the retrieval of quantitative metrics, which in turn challenges the applicability of in vivo 4D-flow MRI for validating simulations[23,38].

We recently reported a flow- and pressure-controlled MRI-compatible setup which embeds subject-specific 3D-printed aortas with compliant walls that is appropriate for comparison with FSI simulations[39,40]. The setup enables direct measurement of all boundary conditions and material parameters, and yields prolonged acquisition times for high-quality 4D-flow MRI data, thus overcoming the technical challenges of studies that deploy a CFD-only approach. Herein, we build upon this work and generate in vitro 4D-flow MRI from three TBAD geometries to establish a comprehensive comparison with FSI simulations (Fig. 1). The objectives of this study were: (1) to evaluate the impact on hemodynamic metrics in TBAD amid variations in entry and exit tear area; and (2) to compare these hemodynamic metrics as obtained from FSI simulations with in vitro 4D-flow MRI.

Methods

Patient-specific model generation

Anatomy and imaging data

A 3D CTA dataset of a 25 year old woman with an uncomplicated TBAD was selected retrospectively from our institutional database. CTA and all other methods were performed in accordance with standard of care procedures. Data retrieval was approved by Stanford University Institutional Review Board (#39377, "Image Registry For Computer Simulations and Image-Based Modeling in Congenital and Acquired Cardiovascular Disease", PI: Alison L. Marsden). The requirement for written consent was waived due to the retrospective nature of the study. Contrast enhanced CTA images were acquired at 1 mm section thickness and 0.7×0.7 mm^2 pixel size from the thoracic inlet to the common femoral arteries. The imaging findings revealed an acute TBAD in the descending thoracic aorta with a dissection flap extending from the left subclavian artery origin down to the distal thoracic aorta, ending above the level of the diaphragm. The proximal entry tear into the false lumen was located immediately distal to the left subclavian artery, and a distal exit tear was located above the diaphragm, superior to the celiac artery origin. The cross-sectional area of entry and exit tear was 228 mm^2 and 227 mm^2, respectively. No branch vessels except for small intercostal arteries branched off of the TL or FL.

Segmentation and digital wall model

A digital model of the patient's thoracic aorta was generated from the CTA dataset. The model included the ascending aorta from above the sinotubular junction, the aortic arch, and the descending thoracic aorta to the level of the diaphragm. The three aortic arch branches were included in the model: brachiocephalic trunk (*BCT*), left common carotid artery (*LCC*), and left subclavian artery (*LSA*). The intercostal arteries were excluded. The model domain was extended to 35 mm distal to the re-entry tear. Two mesh domains were generated: The 'fluid domain'—representing the aortic lumen—was segmented using active contours with manual refinements (itk-SNAP v3.4.0). The 'wall domain'—representing the outer aortic wall and the dissection flap—was extruded from the fluid domain (Autodesk Meshmixer v3.5) with uniform thickness $h = 2$ mm (Fig. 2a). A detailed description of the TBAD model generation is provided in Bäumler et al.[23].

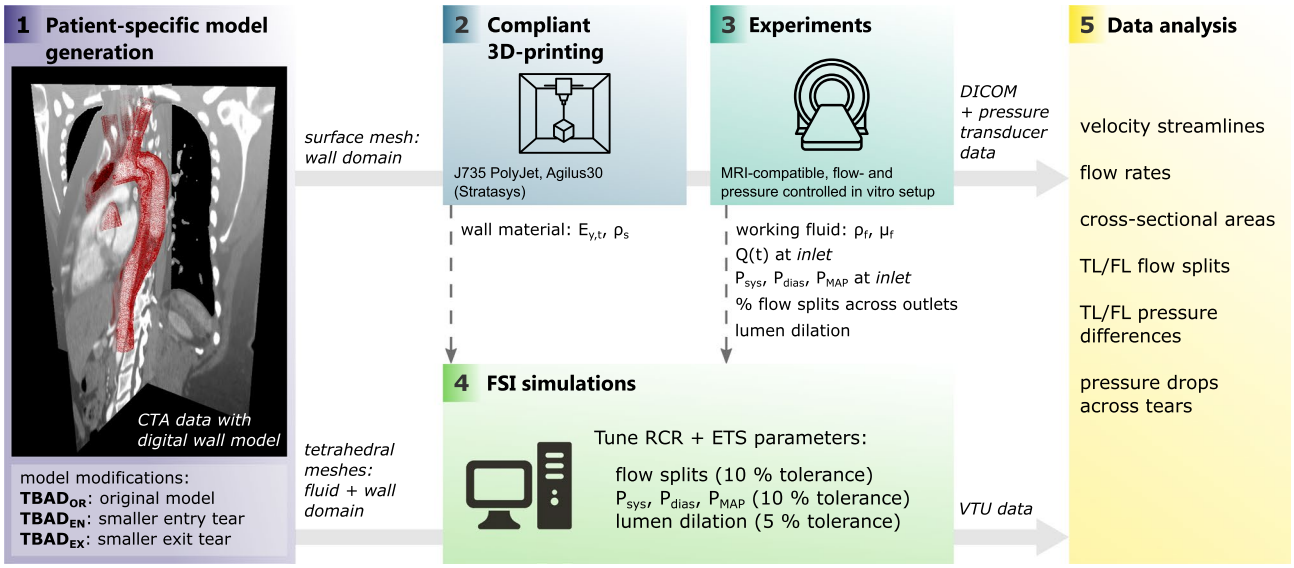

Figure 1. Pipeline showing the key methodological steps: (1) image-based patient-specific model generation from CTA data; (2) compliant 3D-printing; (3) experiments (MRI + catheter-based pressure mapping) with in vitro setup; (4) FSI simulations with boundary conditions informed by measured data (dashed lines); and (5) data analysis, i.e. quantitative and qualitative comparison of hemodynamics between measured and simulated data. CTA: computed tomography angiogram, $Q(t)$: 2D-PC measured net flow, P_{sys}: systolic pressure, P_{dias}: diastolic pressure, P_{MAP}: mean arterial pressure, $E_{y,t}$: tangent Young's modulus wall, ρ_s: density wall, ρ_f: density fluid, μ_f: dynamic viscosity fluid, RCR: Windkessel components, ETS: external tissue support, TL: true lumen, FL: false lumen.

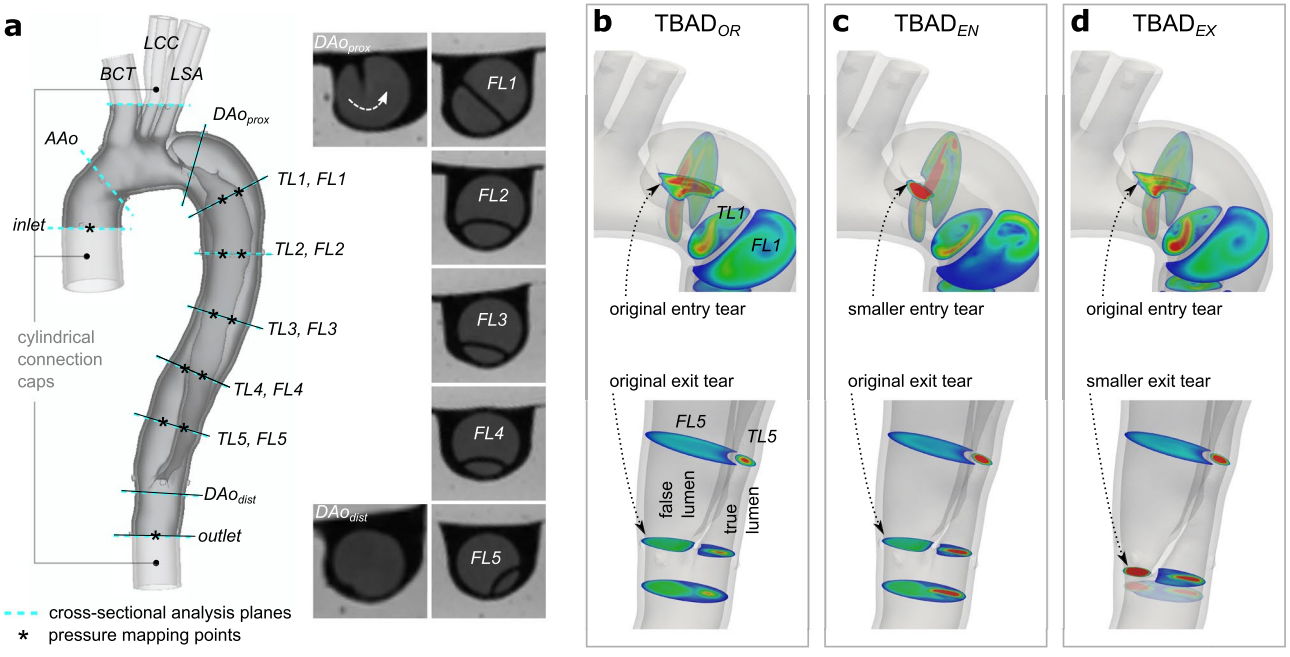

Figure 2. TBAD models. (**a**) Original digital wall model with definition of 18 landmarks that were defined for tuning and analysis purposes. Note that DAo_{prox} cuts through the entry tear, while DAo_{dist} is positioned just below the exit tear. Inset images show 2D-cine MRI frames for cross-sections along the dissected region. Close-up view of entry and exit tear regions for the (**b**) original model $TBAD_{OR}$, (**c**) smaller entry tear model $TBAD_{EN}$, and (**d**) smaller exit tear model $TBAD_{EX}$.

Digital modification of entry and exit tear size

The original patient-specific model $TBAD_{OR}$ was digitally modified to generate two additional models with reduced entry or exit tear size: $TBAD_{EN}$ with reduced entry tear and original exit tear size, and $TBAD_{EX}$ with unchanged entry tear but reduced exit tear size (Fig. 2b,c,d). These local modifications were done manually (using Autodesk Meshmixer v3.5) and were executed such that the existing dissection membrane and vessel wall were not altered and thus did not affect the orientation of the tear, the shape of the two lumen, and the overall shape of the aorta. The smaller size tears were $\approx$ 27% of their original size, measuring 62 mm^2 (entry tear) and 61 mm^2 (exit tear), respectively. All models were augmented with visual landmarks to enable a precise definition of cross-sectional planes for data analysis and comparison. Additionally, the 3D-printed models were augmented with cylindrical caps to facilitate tubing connections. Meshing and model modification tasks were performed using SimVascular[41] and Autodesk Meshmixer.

Compliant 3D-printing

The wall models of $TBAD_{OR}$, $TBAD_{EN}$, $TBAD_{EX}$ were 3D-printed using a stereolithography technique (PolyJet J735, Stratasys Inc.) and a photopolymer print resin (Agilus30, Stratasys Inc.). Printed models were finished with a thin coating film (Bectron, Elantas) to prevent fluid absorption and maintain the material characteristics during the flow experiments. The compliant print material underwent uniaxial tensile testing[39] and proved to be comparable to in vivo aortic wall compliance (tangent Young's modulus $E_{y,t}$ = 1.2 MPa).

Experiments

Flow setup

An MRI-compatible flow setup (Supplementary Fig. S1) was assembled, driven by a programmable pump (CardioFlow 5000 MR, Shelley Medical Imaging Technologies) capable of providing highly-controlled flow and pressure conditions within a physiologic range[39]. In brief, each model was connected to the circuitry tubing via custom designed 3D-printed barbed connectors with tapered transitions (Form 3B, Formlabs Inc.). Each model was then embedded into a solid ballistics gelatin block (ClearBallistics) for stabilization and to provide static MRI signal regions for velocity (phase) offset corrections. The model and gelatin mold were placed inside an enclosed box and connected through box-mounted flow fittings to the periphery. Two capacitance elements controlled the system's downstream compliance, and in turn, pressure waveform amplitude. The net flow splits were adjusted through pinch valves distal to the capacitance elements; an ultrasonic flow sensor (ME-PXL14, Transonic) was used to fine tune the flow splits of the system. The same pinch valves were used to control the outlet resistance and to tune the mean pressure conditions in the system. A pressure transducer (SPR-350S, Millar) was inserted through two ports to record pressure measurements at 12 locations along the model.

Glycerol-water (ratio = 40/60) with added MR contrast medium (ferumoxytol, concentration: 0.75 mL/L) was used as a blood-mimicking fluid with strong T_1 MRI signal enhancement. Fluid density (ρ_f) and dynamic viscosity (μ_f) measurements confirmed ρ_f=1.1 g mm^{-3} and μ_f = 0.0042 Pa s. A typical aortic flow waveform was applied (heart rate = 60/min, stroke volume = 74.1 mL/s, peak flow rate = 300 mL/s, total flow = 4.45 L/min, Supplementary Fig. S1b).

System tuning and pressure mapping

For each of the three models, pressure and flow split conditions were tuned on the MRI scanner table prior to image acquisition. Tuning targets were defined as follows: flow split (outlet vs. combined arch branches) 70/30, inlet systolic pressure (P_{sys}) 120 mmHg or greater, and inlet diastolic pressure (P_{dias}) 70 mmHg or greater. The downstream resistance was reduced in the models with smaller entry or exit tear sizes ($TBAD_{EN}$ and $TBAD_{EX}$ compared to $TBAD_{OR}$) to maintain pressure targets. Once tuning targets were met, luminal pressure data were recorded at twelve locations: one proximal to the dissection, five locations within the TL, five within the FL, and one distal to the dissection (Fig. 2a); three recordings of five consecutive pump cycles (5 s) were obtained per landmark.

MR imaging protocol

MRI acquisitions were performed on a 3T MRI scanner (Skyra, Siemens Healthineers) with a 32-channel spine and 18-channel body matrix coil. The pump provided an external trigger signal to retrospectively gate time-resolved sequences. Image data were acquired immediately after system tuning and pressure mapping.

The protocol included sequences with parameters as follows: (1) 3D spoiled gradient echo (3D-SPGR): voxel size = 1.1 × 1.1 × 1.1 mm^3, FoV = 220 × 123 mm^2, TE = 3 ms, TR = 5.25 ms, flip angle = 25°. 3D-SPGR datasets were acquired under the following conditions: (i) no flow ("flow off") and (ii) steady flow, thus no cardiac gating was applied. (2) 2D phase contrast (2D-PC) at eleven cross-sections (Fig. 2a): pixel size = 1.1 × 1.1 mm^2, slice thickness = 6 mm, FoV = 220 × 123 mm^2, TE = 3 ms, TR = 5.25 ms, flip angle = 25°, averages = 2, V_{enc} = 100–170 cm s^{-1}, retrospective gating (40 frames, temporal resolution = 25 ms). (3) 2D cine gradient echo (2D-cine) at eleven cross-sections (Fig. 2a): pixel size = 0.9 × 0.9 mm^2, slice thickness = 6 mm, FoV = 240 × 150 mm^2 TE = 3 ms, TR = 4.75 ms, flip angle = 7°, averages = 2, retrospective gating (40 frames, temporal resolution = 25 ms). (4) 4D-flow with Cartesian k-space sampling: FoV = 340 × 236 × 84 mm^3, matrix = 220 × 156 × 56, voxel size = 1.5 × 1.5 × 1.5 mm^3, TE = 2.7 ms, TR = 5.6 ms, flip angle = 15°, parallel imaging (GRAPPA, R = 2), V_{enc} = 120–180 cm s^{-1}, lines/segment = 2, retrospective gating (20 frames, temporal resolution = 50 ms). Scan time per model was 1 hour and 30 minutes, and total end-to-end experiment time for all models was 12 h.

FSI simulations

This work's simulation approach was built on previously presented work on FSI simulations in a patient-specific aortic dissection case[23]. To match the experimental conditions for the present study, the following adaptations were made: (i) we prescribed homogeneous material properties throughout the structural domain, i.e. no distinction between intimal flap and outer material wall properties; (ii) prestress of the structural domain was set to zero.

Mesh generation

For each geometric model ($TBAD_{OR}$, $TBAD_{EN}$, and $TBAD_{EX}$) we created refined unstructured tetrahedral meshes with the TetGen mesh generator[42] (embedded in SimVascular[41]). Based on previous simulations, a mesh size of 1.3 mm was found to be sufficiently small[23]. Each mesh consisted of approximately 1.1×10^6 tetrahedral elements for the fluid domain and approximately 0.5×10^6 tetrahedral elements for wall domain.

Governing equations

The fluid flow was governed by the Navier–Stokes equations with viscosity $\mu_f = 0.0042$ Pa s and density $\varrho_f = 1100$ kg m^{-3}. The FSI equations were formulated in arbitrary Lagrangian–Eulerian (ALE) coordinates[23,43], which allowed us to capture the coupled motion of the fluid and structural domain using a finite element method (described below). Both glycerol and water are Newtonian fluids. To closely approximate the fluid behavior we therefore modeled the fluid as Newtonian and incompressible. The 3D printed material representing the arterial wall was modeled as a homogeneous, isotropic, nonlinear, hyperelastic material, and described by a Neo–Hookean material model[43]. Structural density (per manufacturer's spec sheet) and elasticity (as measured) were $\varrho_s = 1450$ kg m^{-3} and $E_{y,t} = 1.2$ MPa, respectively. To account for the presence of the gelatin mold surrounding the printed models we applied external tissue support (ETS) to the outer arterial wall in the form of a Robin boundary condition[44]:

$$\boldsymbol{\sigma_S n} = -k_S \boldsymbol{u_S} - c_S \partial_t \boldsymbol{u_S} - p_0 \boldsymbol{n}, \tag{1}$$

where $\boldsymbol{\sigma_S}$ denotes the Cauchy stress tensor of the structural domain, $\boldsymbol{n}$ the unit outer normal vector, $\boldsymbol{u_S}$ the displacement field, and p_0 the external (or intrathoracic) pressure. The user-defined scalar parameters k_S and c_S denote the elastic and viscoelastic response of the external tissue, respectively.

Boundary data and tuning

At the model inlet we prescribed a pulsatile flow waveform that was informed from in vitro 2D-PC MRI measurements; a parabolic velocity profile was used. At the four model outlets, we applied three-element Windkessel boundary conditions which account for downstream vascular effects[45]. The total resistance R_T and capacitance C_T were tuned and distributed across all outlets such that every outlet i was described by a proximal resistance $R_{P,i}$, distal resistance $R_{D,i}$, and capacitance C_i. The ratio of distal to proximal resistance k_d was fixed for each model, and the distribution of total resistance and capacitance were governed by the experimentally determined flow splits. Details of the tuning process have been described in Bäumler et al.[23]. The target pressure values comprised systolic pressure (P_{sys}), diastolic pressure (P_{dias}), and mean pressure (P_{MAP}) values—informed by experimental pressure mapping. Target flow ratios across outlets *BCT*, *LCC*, *LSA*, and *outlet* were informed by 2D-PC net flow measurements. Tuning targets (Table 1) were matched with relative residual errors of ≤1.4%, ≤4.1% and ≤ 4.6% for pressure and ≤ 3.4%, ≤ 7.4% and ≤ 7.3% for flow splits (corresponding to $TBAD_{OR}$, $TBAD_{EN}$, and $TBAD_{EX}$, respectively)

ETS parameters k_S and c_S were chosen such that the FSI-simulated minimum-to-maximum lumen dilation at *AAo* matched the MRI-measured minimum-to-maximum dilation in the 3D-printed models. ETS tuning

		Pressure tuning at *inlet*				Flow split tuning across outlets			
		P_{sys}	P_{dias}	P_{MAP}		*BCT*	*LCC*	*LSA*	*outlet*
$TBAD_{OR}$	Simulated (mmHg)	127.5	59.1	86.1	Simulated (%)	15.5	3.2	5.6	75.7
	Measured (mmHg)	126.4	60.0	86.1	Measured (%)	15.0	3.1	5.4	76.5
	Residual error (%)	0.82	1.42	0.08	Residual error (%)	3.37	3.22	3.08	1.02
$TBAD_{EN}$	Simulated (mmHg)	141.9	72.7	95.7	Simulated (%)	12.3	3.0	6.1	78.6
	Measured (mmHg)	137.7	69.9	96.2	Measured (%)	11.4	2.8	5.7	80.1
	Residual error (%)	3.02	4.11	0.57	Residual error (%)	7.43	7.21	7.00	1.84
$TBAD_{EX}$	Simulated (mmHg)	148.6	75.1	100.4	Simulated (%)	11.7	3.3	5.0	80.1
	Measured (mmHg)	142.1	73.5	98.9	Measured (%)	10.9	3.1	4.6	81.4
	Residual error (%)	4.58	2.24	1.5	Residual error (%)	7.26	7.06	6.93	1.63

Table 1. Inlet pressure (mmHg) and flow splits (% of total outflow) for the three models. The FSI simulations matched target pressure values (systolic (P_{sys}), diastolic (P_{dias}), and mean (P_{MAP})) with a relative error of ≤ 4.58% and absolute error of ≤ 6.5 mmHg. Flow split ratios between outlets were matched in the FSI simulations with a relative error of ≤ 7.43% and an absolute error of ≤ 1.5%.

yielded a relative dilation of 5.0%, 5.0% and 5.3% in FSI compared to 4.4%, 5.0% and 5.4% in 2D-cine MRI (for $TBAD_{OR}$, $TBAD_{EN}$, and $TBAD_{EX}$, respectively). Tuning parameter settings and pressure traces are provided in Supplementary Table S2 and Supplementary Fig. S3, respectively.

Numerical solver

The governing equations were solved with the open source finite element solver svFSI (SimVascular[41,46]). svFSI features a second order generalized α-time stepping scheme, linear tetrahedral elements for pressure and velocity (with pressure and momentum stabilization), two-way coupling of the fluid and structural domain, pre-conditioning of the resulting linear systems, and backflow stabilization at the fluid outlets[47–49]. To assure periodicity of the simulation, at least 6 cardiac cycles were simulated before results were extracted for the final cycle. The simulations were carried out on two nodes (Intel(R) Xeon(R) Gold 5118, 2.30 GHz) with a total of 48 CPUs; approximate runtime was 10 h per cardiac cycle.

Data analysis

For MRI data, TBAD lumen segmentation was performed on high-resolution 3D-SPGR steady flow data (using watershed-based region-growing) and facilitated image-based flow visualization. 2D-cine datasets were used to automatically track through-cycle aortic wall and flap deformation[50] and to compute cross-sectional area change. 2D-PC datasets were corrected for velocity (phase) offsets and processed to retrieve the inlet flow rate waveform as well as percentage net flow splits across outlets. 4D-flow datasets were corrected for the following conditions: (i) Maxwell terms (during MR reconstruction), (ii) gradient non-linearity distortion[51], and (iii) phase offsets. 4D-flow datasets were reformatted at each analysis location (Fig. 2a) to generate cross-sectional phase and magnitude images. Reformatted magnitude images were used to track lumen boundaries which served to calculate quantitative flow parameters based on reformatted phase images. Post-processing of the MRI data was completed using MevisLab modules (v3.5a, Fraunhofer Institute for Digital Medicine) and ParaView (v5.7, Kitware). Pressure measurements were analyzed using dedicated data acquisition system software (LabChart 8, ADInstruments) and pressure signals were averaged over five cardiac cycles. FSI simulation results were exported as VTK unstructured grid files (.vtu) from svFSI at 80 time-steps over a single cardiac cycle (i.e. temporal frame length: 12.5 ms). Qualitative visualization and quantitative analysis of simulated datasets were performed using ParaView (v.5.7, Kitware).

Results

Flow patterns

Each of the three models exhibited a unique flow pattern and velocity distributions, with excellent qualitative agreement between 4D-flow MRI and FSI simulations (Figs. 3, 4, and Supplementary Videos S4–S8). Highly complex and distinct flow patterns were observed in the proximal false lumen adjacent to the entry tear region. A high-velocity flow jet through the entry tear with impingement on the opposite FL wall was only observed in the $TBAD_{EN}$ model. The impingement zone was also associated with a steep local pressure gradient affecting the FL wall (Fig. 4c). Helical flow patterns were also visible in the proximal TL close to the entry tear and were well captured by both techniques (Fig. 3b). In the distal part of the dissected descending aorta, the modified models, $TBAD_{EN}$ and $TBAD_{EX}$, showed increased flow velocities in the TL (Fig. 3a, arrows), which was consistent with the higher TL net flow volumes in these models, as reported below. In addition, $TBAD_{EX}$ showed increased velocity through the exit tear compared to the $TBAD_{OR}$ and $TBAD_{EN}$ models. The smaller exit tear in the $TBAD_{EX}$ model also caused reversed flow distal to the exit tear (Fig. 3c, Supplementary Video S8), whereas $TBAD_{OR}$ and $TBAD_{EN}$ showed unidirectional laminar flow in this region. During diastole, additional flow oscillations through the entry tear (in particular for $TBAD_{EN}$, Fig. 4b), and persistent helical flow in FL (Supplementary Videos S6, S7) were observed.

Flowrate measurements

FL flow ratio

The FL flow ratio (FR_{FL}, in %) was defined based on the TL and FL net flow volumes ($\overline{Q}_{TL}$, $\overline{Q}_{FL}$) as:

$$FR_{FL} := \frac{\overline{Q}_{FL}}{\overline{Q}_{FL} + \overline{Q}_{TL}} * 100. \tag{2}$$

FR_{FL} was substantially decreased in the modified tear models, $TBAD_{EN}$ and $TBAD_{EX}$, compared to the original $TBAD_{OR}$ model. Specifically, FR_{FL} was 73.7%, 55.2% and 56.4% for 4D-flow MRI and 77.6%, 59.8% and 61.6% for FSI simulations (values given for $TBAD_{OR}$, $TBAD_{EN}$, and $TBAD_{EX}$, respectively).

Dynamic flowrates over the cardiac cycle

Transient flow rates at multiple cross-sectional landmarks showed higher systolic peaks in FSI simulations, whereas higher diastolic flow was observed in 4D-flow MRI (Fig. 5a). Damping of the flow waveform from DAo_{prox} to DAo_{dist} as well as along the individual lumina was observed in all three models, with stronger damping in 4D-flow and 2D-PC data than in FSI simulations. Diastolic flow oscillations were most pronounced in FSI simulations, with short periods of reverse (i.e. negative) flow at $t \approx 500$ ms. To further assess potential underestimation of systolic flow in 4D-flow MRI, 2D-PC measurements at identical locations were added to Fig. 5a.

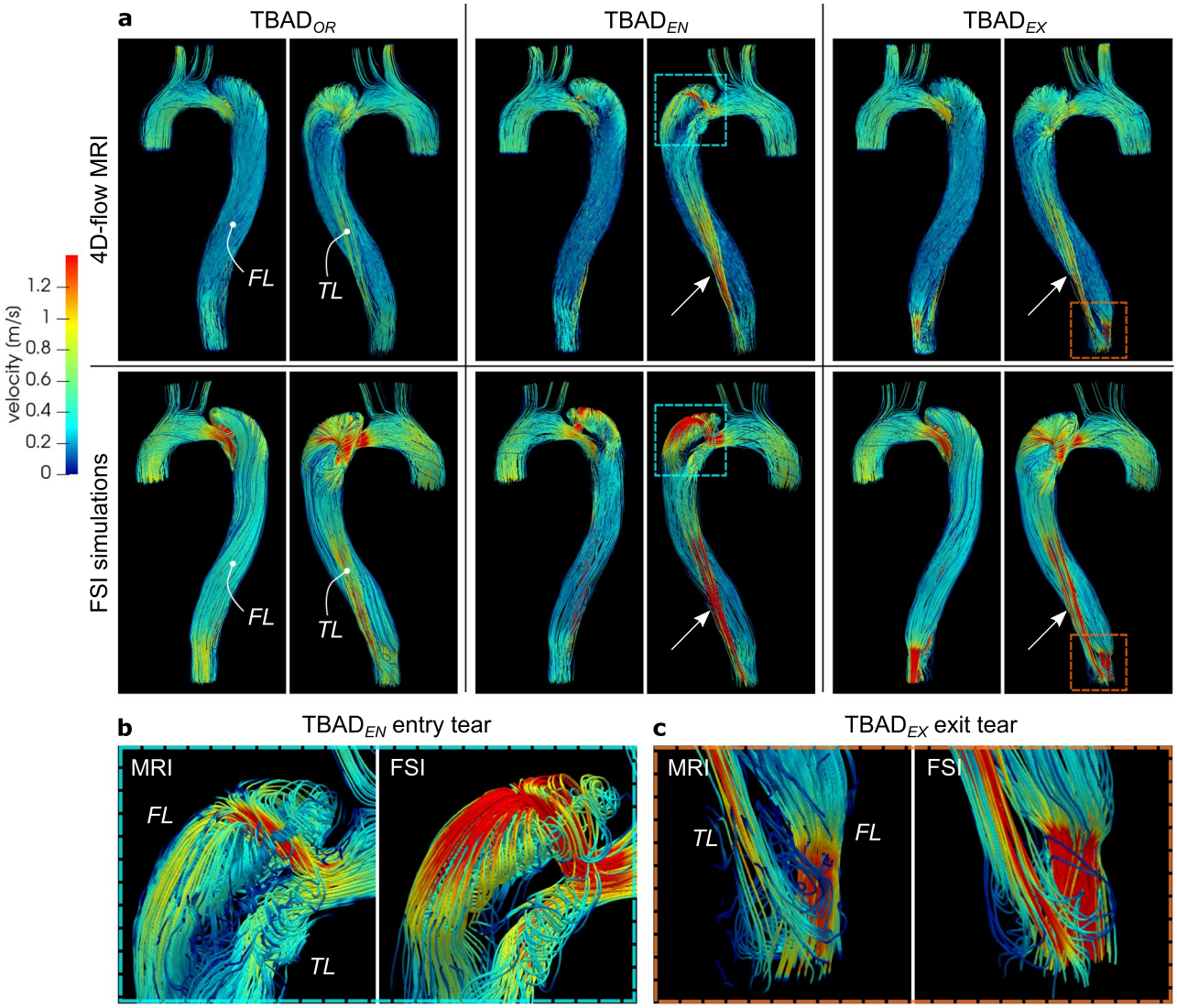

Figure 3. (**a**) Streamlines at peak systole (t= 200 ms) rendered from 4D-flow MRI (top) and FSI-simulated (bottom) data. Each model exhibits unique local flow characteristics that are in agreement between techniques. Key observations include: (i) increased flow velocities through the entry tear region, particularly in $TBAD_{EN}$, and local helical flow in the proximal TL and FL in the vicinity of the entry tear (blue box, close-up view in (**b**)); (ii) increased TL flow velocity for the modified $TBAD_{EN}$ and $TBAD_{EX}$ models (arrows); (iii) flow jet through small size exit tear in $TBAD_{EX}$, with recirculating TL flow distal to the exit tear (orange box, close-up view in (**c**)). Graphics created using ParaView (v5.7, https://www.paraview.org).

Cross-sectional area measurements

The cross-sectional lumen area was evaluated as absolute area, and as relative area changes over the cardiac cycle. For the latter, the first frame was used as the end-diastolic reference for normalization. In addition to area measurements during pulsatile flow, we also obtained absolute area values from the STL model file, from both "flow-off" and steady flow MRI imaging datasets, and from steady flow FSI simulations. These additional measurements were all based on the $TBAD_{OR}$ model.

Absolute area measurements

FSI simulations, compared to 2D-cine MRI based wall contour tracking, resulted in smaller absolute cross-sectional area at the majority of landmarks (Fig. 6b). Specifically, FSI-based area measurements in peak-systole and end-diastole (mean ± SD) differed from MRI-based values by (− 16.6 ± 10.5)%, (− 7.0 ± 11.2)% and (− 3.1 ± 12.2)% for $TBAD_{OR}$, $TBAD_{EN}$, and $TBAD_{EX}$ respectively. Additional "flow-off" experiments showed acceptable agreement with STL-based values (− 4.7% ± 16.1%), but measurements during steady flow affirmed smaller absolute cross-sectional areas of the simulated deformable wall domain than in the printed model (− 0.6% ± 10.4%). Numerical results for all area measurements are listed in Supplementary Table S9 and plotted in Supplementary Fig. S10.

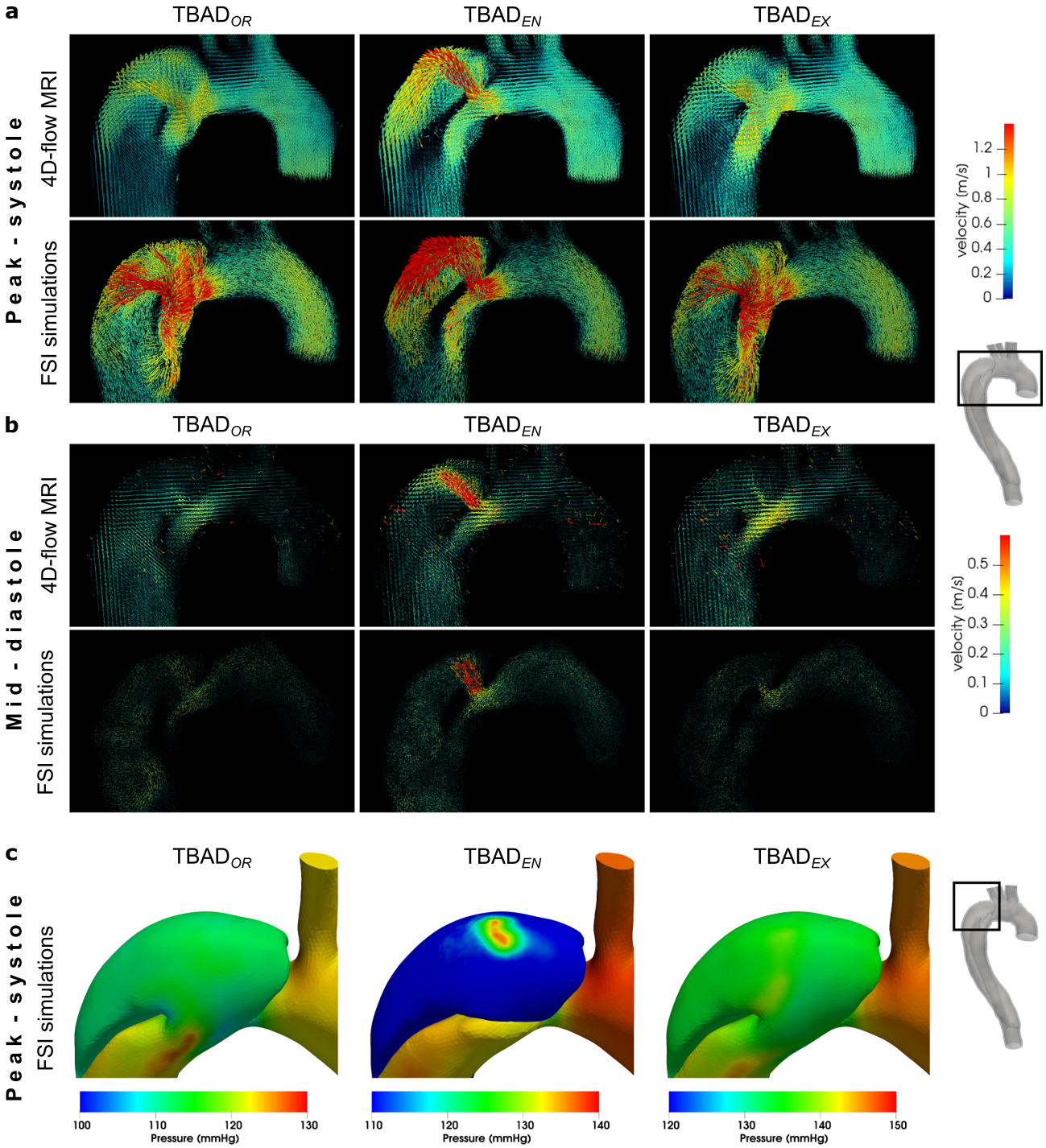

Figure 4. Flow and pressure dynamics in the arch region. Velocity vectors in the aortic arch at (**a**) peak systole (t= 200 ms) (**b**) and mid-diastole (t= 600 ms) based on 4D-flow MRI data and FSI simulations. During systole, flow patterns are in agreement between both modalities and for each model, but velocities are higher in FSI simulations. Mid-diastole renderings reveal a secondary push through the entry tear, that is most pronounced in $TBAD_{EN}$. For full-cycle animations refer to Supplementary videos 1–5. (**c**) Absolute pressure at the lumen boundary (t = 250 ms) from the FSI simulations. $TBAD_{EN}$ shows a local pressure difference of ≈ 35 mmHg in the FL impingement zone. Graphic created using ParaView (v5.7, https://www.paraview.org).

Relative area changes over cardiac cycle

Figure 5b displays transient curves of relative cross-sectional areas for $TBAD_{OR}$, $TBAD_{EN}$, and $TBAD_{EX}$: TL areas increased by a factor of up to 1.02, 1.04 and 1.03 in the experiments and up to 1.03, 1.06 and 1.03 in FSI

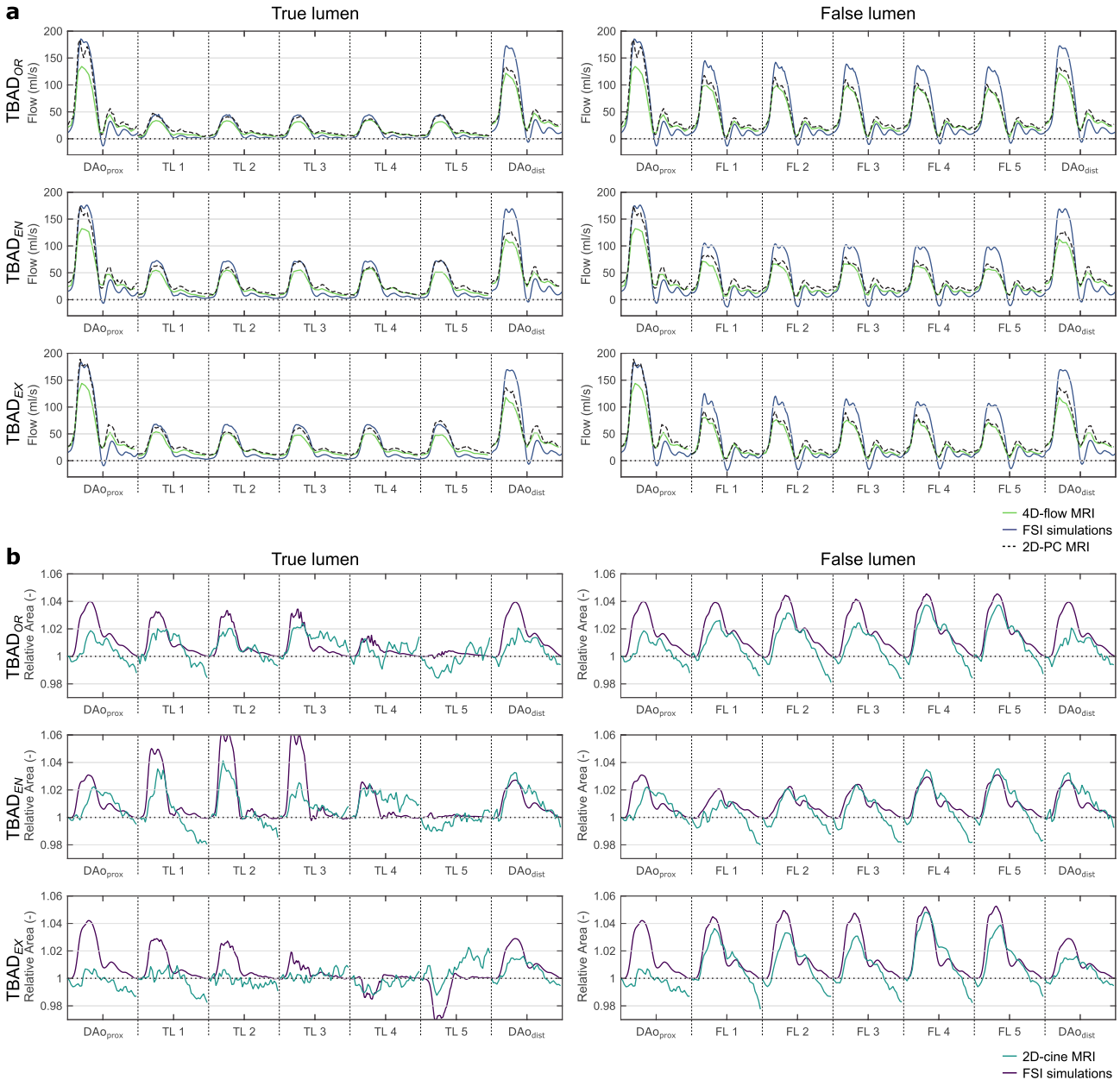

Figure 5. (**a**) Flow rates over the cardiac cycle along the dissected descending aorta based on 4D-flow MRI (green), FSI simulations (blue), and 2D-PC MRI (black, dashed). (**b**) Cross-sectional area over the cardiac cycle based on 2D-cine MRI (light blue) and FSI simulations (purple). Relative area change was defined as absolute area divided by area in the first cycle frame. For landmark label definition see Fig. 2a.

simulations over the cardiac cycle. FL areas increased by a factor of up to 1.04, 1.04, and 1.05 in experiments and up to 1.05, 1.03 and 1.05 in FSI simulations for $TBAD_{OR}$, $TBAD_{EN}$, and $TBAD_{EX}$, respectively. TL in $TBAD_{EX}$ showed a slight collapse at the distal landmarks *TL4* ($\approx -1\%$) and *TL5* ($\approx -3\%$), as captured best in FSI simulations; 2D-cine MRI data did not fully reveal this behavior.

Pressure

Pressure drops along centerline

Peak-systolic pressure (P_{sys}) at twelve pressure mapping landmarks was normalized with respect to the peak-systolic pressure at *inlet* (Fig. 6a). Overall, *inlet* to *outlet* pressure drops were smallest in the original $TBAD_{OR}$ model (2% and 7%), and larger for the modified $TBAD_{EN}$ (9% and 20%) and $TBAD_{EX}$ (18% and 19%); given value pairs correspond to experiments and FSI simulations.

Pressure drop across the entry tear (i.e. TL entering FL, see *inlet* to *FL1*) was largest in $TBAD_{EN}$, with a decrease of 17% and 20% in experiments and FSI simulations, respectively. Pressure drop across the exit tear (i.e. FL merging back into the TL, see *FL5* to *outlet*) was largest in $TBAD_{EX}$, with a pressure decrease by 11% and 14% in experiments and FSI simulations, respectively.

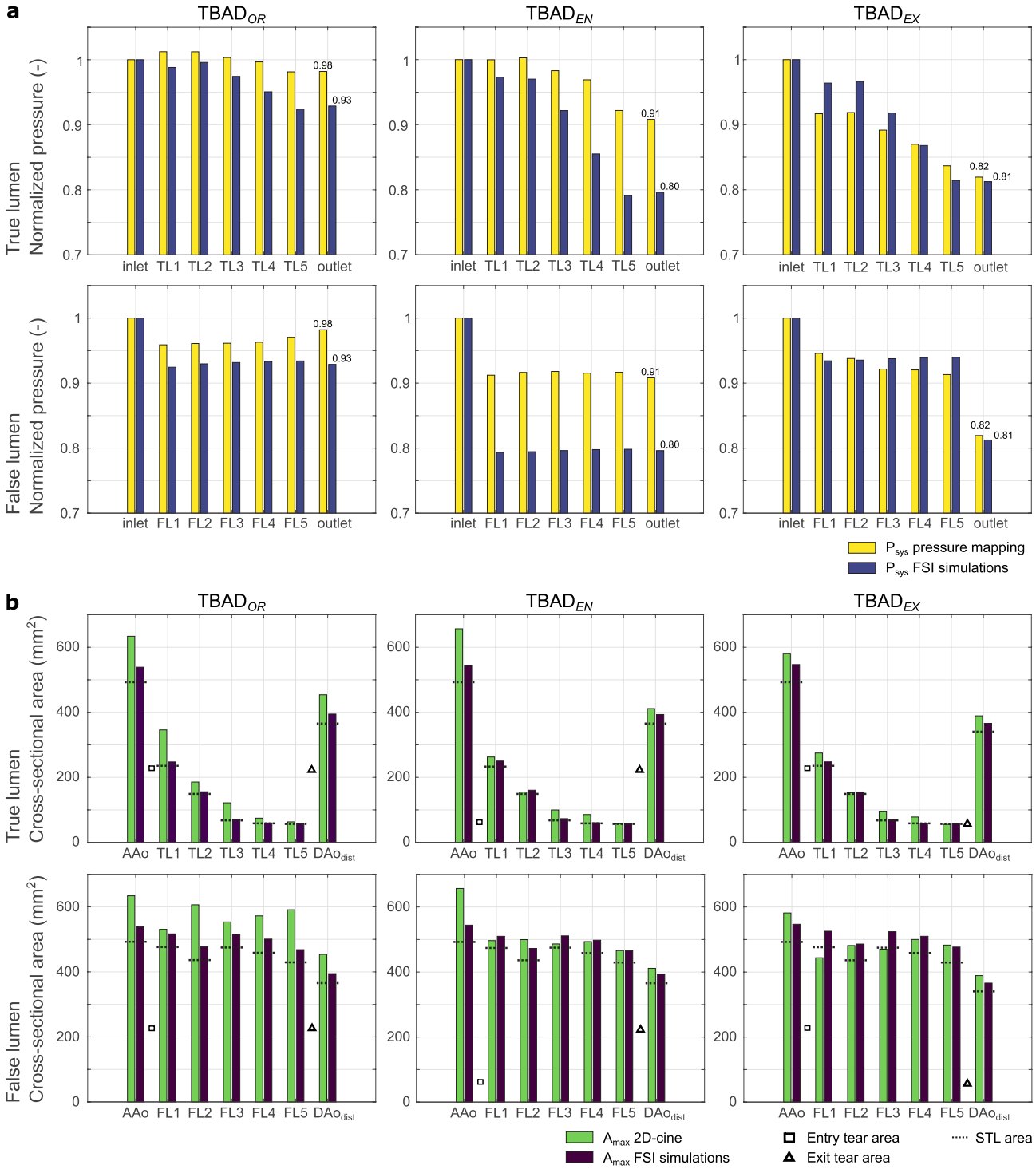

Figure 6. (**a**) Relative pressure (i.e. normalized to peak pressure at *inlet*) drops along the aortic centerline including *inlet*), *outlet*), as well five landmarks in both the TL and FL. (**b**) Maximum cross-sectional area measurements at the identical landmarks used for pressure mapping, except for *AAo*, which was chosen over 'inlet', since *inlet* is fixed both in the 3D-printed model and in the simulation setup. Dashed bars denote area values obtained from the STL model file, squares denote size of entry tear, and triangles denote size of exit tear. For landmark label definition see Fig. 2a.

For all models, peak-systolic pressure did not drop noticeably along the FL centerline (*FL1* to *FL5*). However, pressure values steadily decreased along the TL (*TL2* to *TL5*), with the strongest TL pressure decline observed in $TBAD_{EX}$ (15% and 20% in the experiments and FSI simulations, respectively). The largest discrepancy between

experimental pressure measurements and FSI simulations was found in the $TBAD_{EN}$ model, particularly in the FL. Here, *inlet* to FL pressure (at *FL1*) dropped by ≥ 20% in FSI simulations, but ≤ 10% in the experiments.

TL-FL pressure differences

Inter-luminal pressure differences were calculated as

$$\Delta P_{TL-FL} := P_{TL} - P_{FL} \tag{3}$$

at five locations along the dissected aorta. $\Delta P_{TL-FL}$was substantially affected by tear size and steadily decreased from proximal to distal locations (Fig. 7). $\Delta P_{TL-FL}$was positive at all landmarks and throughout the cardiac cycle for $TBAD_{OR}$ and $TBAD_{EN}$, with maximum systolic differences of (7.9, 11.0) mmHg for $TBAD_{OR}$ and (14.6, 28.9) mmHg for $TBAD_{EN}$. $TBAD_{EX}$ FL pressure exceeded TL pressure by up to (13.2, 20.6) mmHg during systole; values are given for catheter-based and simulated data, respectively.

At end-diastole, FSI-simulated TL and FL pressures were in approximate equilibrium (-0.5 mmHg< ΔP_{TL-FL} < 1 mmHg), whereas experimental pressure measurements resulted in $\Delta P_{TL-FL} \neq 0$. Inter-luminal diastolic pressure differences measured slightly positive for the $TBAD_{OR}$ and $TBAD_{EN}$ models (0.9 mmHg< ΔP_{TL-FL} < 3.2 mmHg), and negative for the $TBAD_{EX}$ model (− 7.6 mmHg< ΔP_{TL-FL} < − 5.5 mmHg).

Discussion

Hemodynamic factors—together with biomechanical, mechanobiological, genetic, and morphological factors—underlie the development and progression of aortic dissection and are being investigated as biomarkers for prognosis and treatment decisions. The complex interplay between these factors is incompletely understood, and evolving computational methods to obtain patient-specific hemodynamic must be rigorously validated. The present study assessed the hemodynamic effects of entry and exit tear size variations in a patient-specific TBAD model using two modalities. We directly compared hemodynamic features of FSI simulations against in vitro MRI and catheter-based pressure data in compliant 3D-printed TBAD models. The in vitro approach enabled the study of quantitative hemodynamics in a highly controlled environment and without a scan time limitation. Moreover, the experiments informed the boundary conditions and material parameter specifications in the FSI simulations with catheter-based pressure data and high fidelity material property estimates, which are not typically available in any clinical setting[23].

Local and global flow helices, recirculation zones, and flow jets through tears were visualized in fine detail via streamlines, and were well captured in both 4D-flow MRI and FSI simulations. In particular, local helices in the vicinity of the entry tear (Fig. 3b, $TBAD_{EN}$) and distal to the exit tear (Fig. 3c, $TBAD_{EX}$) are strikingly similar using both techniques. The emergent entry tear flow jet in $TBAD_{EN}$ impinging on the opposite FL wall, creating a local pressure gradient was equally demonstrated by 4D-flow MRI and FSI (Fig. 4a). This impingement zone may promote tissue degradation and destructive remodeling via mechanobiological pathways and potentially lead to aneurysmal degeneration[52,53].

Comparing results between both modalities (FSI and MRI), in systole, FSI simulations displayed overall higher flow velocities, whereas in diastole, 4D-flow measured higher velocities. Similarly, simulated flow rates

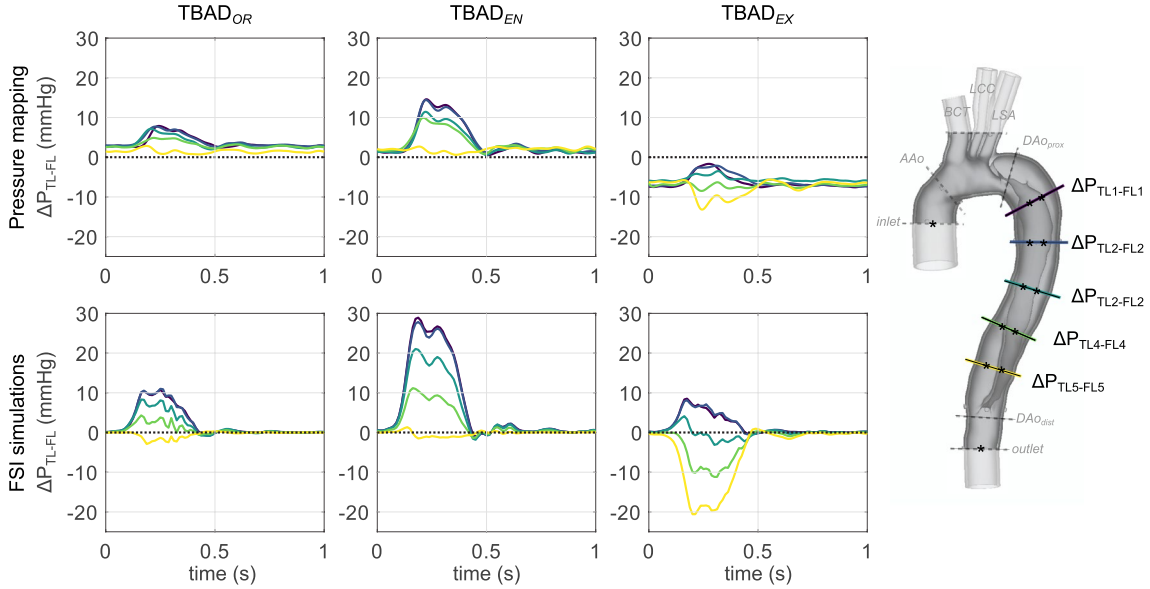

Figure 7. Inter-luminal pressure difference ΔP_{TL-FL} between TL and FL according to pressure transducer measurements (top) and FSI simulations (bottom). ΔP_{TL-FL} increased when the entry tear was made smaller ($TBAD_{EN}$), and decreased—including negative pressure difference at distal landmarks—when exit tear made smaller ($TBAD_{EX}$).

were higher in systole and lower in diastole when compared to MRI data, specifically in 4D-flow MRI (Fig. 5a). Two confounding effects may explain this result: First, there is general consensus that 4D-flow MRI underestimates peak velocities when compared to 2D-PC MRI. Our results confirm that 2D-PC MRI consistently resulted in higher peak velocities, and therefore showed smaller discrepancies with FSI simulations. Second, less dampening seems to occur in FSI simulations. This is nicely reflected by the initially well matched flow rates (between 2D-PC and FSI) at landmark *inlet*, but then higher systolic and lower diastolic flow (for FSI simulations) at all downstream landmarks.

Entry and exit tear size considerably affected inter-luminal pressure differences and true and false lumen flow splits. Peak-systolic ΔP_{TL-FL} was positive in the $TBAD_{OR}$ model (up to 11.0 mmHg), then further increased in the reduced entry tear model (up to 28.9 mmHg), but flipped to negative in the reduced exit tear model (up to − 20.6 mmHg). Additionally, both of the tear-modified models significantly reduced FR_{FL} down to 75% of the initial $TBAD_{OR}$ value. This drastic FR_{FL} reduction indicates that the flow throughput is dictated by the total resistance and independent of the location of the narrowing. Consequently, it appears that despite the decrease in FR_{FL} an increase in outflow resistance—which only occurred in the $TBAD_{EX}$ model—contributes to FL pressurization, which is thought to promote FL degeneration and aneurysm formation.

Inter-modality comparison showed overall acceptable agreement for ΔP_{TL-FL}. Both FSI simulations and catheter-based measurements link a small exit tear to false lumen pressurization, which is hypothesized to increase the risk for late adverse events in TBAD patients. Moreover, our results align with findings by Cuellar-Calabria et al.[21], who identified "entry tear dominance" (here: $TBAD_{EX}$ model) as a predictor of late adverse events. Absolute numbers for FSI-derived ΔP_{TL-FL} deviated from catheter-based measurements and showed (1) greater systolic inter-luminal pressure gradients, and (2) diastolic inter-luminal pressure equilibrium at all landmarks, rather than $\Delta P_{TL-FL} \neq 0$ in catheter-based measurements. To explain these effects, we revisited potential causes as follows: differences of actual tear size between the 3D-printed model and the digital wall model, wall and fluid mesh coarseness distal to the exit tear, and catheter-based measurement inaccuracies relative to measured ΔP_{TL-FL}. But, none of these additional analyses led to a sound explanation as to why these discrepancies occured.

Tear size alterations also affected peak-systolic pressure drops along the luminal centerline. First, simulated and measured data agreed on substantially greater *inlet* to *outlet* pressure drops in both of the tear-modified models. Similar trends that describe increased pressure drops have been reported for aortic coarctation[54,55], which refers to a focal narrowing of the proximal descending aorta. Second, the modification of tear size led to different locations of the steepest pressure drop along the centerline (Fig. 6). $TBAD_{EN}$ exhibited the largest gradient across the entry tear; whereas $TBAD_{EX}$ exhibited the largest gradient across the exit tear. Although simulated data presented larger pressure drops between centerline locations, relative trends again were well-matched between modalities.

In addition to the effect of entry and exit tear sizes, our results also showcase the relationship between the cross-sectional luminal area and the P_{sys} drops along the respective luminal centerlines. Along the TL centerline, P_{sys} decreased incrementally, while the cross-sectional area narrowed considerably further downstream—that is, the area at *TL5* was 24% of the area at *TL1*. In comparison, our results suggest no considerable drop of P_{sys} along the FL centerline, along which cross-sectional area values remained approximately constant.

The combined results for ΔP_{TL-FL} and relative area change over the cardiac cycle also revealed the well known clinical phenomenon of TL compression and collapse. If only FSI simulation are considered, one can deduce: $\Delta P_{TL-FL} > 0$ caused an increase in TL area, $\Delta P_{TL-FL} \approx 0$ was reflected by negligible area change (that is, constant area through the cycle), and $\Delta P_{TL-FL} < 0$ (as observed in the $TBAD_{EX}$ model only) caused a decrease in TL area, corresponding to a compression of the TL. Area measurements from 2D-cine MRI also hint at potential TL collapse in the $TBAD_{EX}$ model.

Three limitations of the present study should be addressed. First, several assumptions simplified the actual TBAD in vivo scenario: Both experiments and simulations utilized a uniform thickness and elasticity for the outer aortic wall and the dissection flap. Thus, we are unable to analyze effects of spatially varying or non-isotropic wall characteristics on hemodynamics. The FSI simulations also did not pre-stress the wall domain. While this matches the in vitro measurements for a 3D-printed models, any study that considers inherently pre-stressed in vivo tissue and data may require incorporation pre-stress effects[23]. In addition, the ETS modeling parameters in the FSI simulations were applied uniformly. Both the presented in vitro embedding of the models, and likely also the surrounding of the thoracic aorta in vivo, is expected to non-uniformly restrict the movement of the outer aortic wall. We also acknowledge that blood is a non-Newtonian fluid with shear-thinning properties, especially prominent in regions with low shear rates[56,57]. However, we used a Newtonian fluid in the experimental setup and therefore modeled the fluid as Newtonian in the simulations to facilitate the direct comparison.

Second, retrieving precise wall deformation measurements of the 3D-printed models was limited by 2D-cine MRI spatial resolution as well as the inherent error of the registration-based wall tracking algorithm. Specifically, this affected area measurements in the relatively small-sized TL. While obtaining structural motion from FSI simulations can be considered error-free, measuring area based on the given 2D-cine MRI is not. Future works must refine methods for measuring wall and flap motion in the experimental setup.

Lastly, this study investigated only a single TBAD case with its unique patient-specific features; specifically, no fenestration points (that is, additional small communications between the TL and FL along dissection flap) were present, the dissection did not extend distal to the celiac trunk, and—for feasibility purposes—we excluded intercoastal arteries when building the model. Novel advances in 3D printing, specifically the integration of tissue mimicking materials, provide excellent versatility in model manufacturing regarding global and local geometry, thickness and elasticity—a technical tool that could be leveraged in future works.

In conclusion, this work describes changes in the TBAD hemodynamics due to tear size alterations while comparing results from in vitro MRI and pressure mapping experiments with FSI simulations. In particular, the results demonstrate FL pressurization owing to a decreased exit tear size—with well-matched observations

between measurements and simulation. The present study contributes to a better understanding of the interplay between TBAD morphology and associated quantitative hemodynamics.

Data availibility

TBAD model files (.stl), MRI data (.dcm), pressure traces (.csv), and FSI-simulated data (.vtu) are publicly available through Stanford Digital Repository "TBADFlow": https://purl.stanford.edu/tz375fg1985.

Received: 5 January 2023; Accepted: 13 December 2023
Published online: 18 December 2023

References

1. Fleischmann, D. *et al.* Imaging and surveillance of chronic aortic dissection: A scientific statement from the American Heart Association. *Circ. Cardiovasc. Imaging* **15**, 200–221. https://doi.org/10.1161/HCI.0000000000000075 (2022).
2. Nienaber, C. A. *et al.* Aortic dissection. *Nat. Rev. Dis. Primers* **2**, 16053. https://doi.org/10.1038/nrdp.2016.53 (2016).
3. Chiu, P. & Miller, D. C. Evolution of surgical therapy for Stanford acute type a aortic dissection. *Ann. Cardiothor. Surg.* **5**, 275–295. https://doi.org/10.21037/ACS.2016.05.05 (2016).
4. Pape, L. A. *et al.* Presentation, diagnosis, and outcomes of acute aortic dissection: 17-year trends from the international registry of acute aortic dissection. *JACC* **66**, 350–358. https://doi.org/10.1016/J.JACC.2015.05.029 (2015).
5. Afifi, R. O. *et al.* Outcomes of patients with acute type B (DeBakey III) aortic dissection: A 13-year, single-center experience. *Circulation* **132**, 748–754. https://doi.org/10.1161/CIRCULATIONAHA.115.015302 (2015).
6. Isselbacher, E. M. *et al.* 2022 ACC/AHA guideline for the diagnosis and management of aortic disease: A report of the American Heart Association/American College of Cardiology Joint Committee on Clinical Practice Guidelines. *Circulation* **146**, 334–482. https://doi.org/10.1161/cir.0000000000001106 (2022).
7. Schwartz, S. I. *et al.* Predictors of late aortic intervention in patients with medically treated type B aortic dissection. *J. Vasc. Surg.* **67**, 78–84. https://doi.org/10.1016/J.JVS.2017.05.128 (2018).
8. Spinelli, D. *et al.* Current evidence in predictors of aortic growth and events in acute type B aortic dissection. *J. Vasc. Surg.* **68**, 1925–35. https://doi.org/10.1016/j.jvs.2018.05.232 (2018).
9. Kunishige, H. *et al.* Predictors of surgical indications for acute type b aortic dissection based on enlargement of aortic diameter during the chronic phase. *Jpn. J. Thorac. Cardiovasc. Surg.* **54**, 477–482. https://doi.org/10.1007/S11748-006-0039-9 (2006).
10. Tsai, T. T. *et al.* Partial thrombosis of the false lumen in patients with acute type B aortic dissection. *NEJM* **357**, 349–359. https://doi.org/10.1056/NEJMoa063232 (2007).
11. Sailer, A. M. *et al.* Computed tomography imaging features in acute uncomplicated Stanford type-B aortic dissection predict late adverse events. *Circ. Cardiovasc. Imaging* **10**, e005709. https://doi.org/10.1161/CIRCIMAGING.116.005709 (2017).
12. Lavingia, K. S. *et al.* Volumetric analysis of the initial index computed tomography scan can predict the natural history of acute uncomplicated type B dissections. *J. Vasc. Surg.* **62**, 893–899. https://doi.org/10.1016/J.JVS.2015.04.449 (2015).
13. Evangelista, A. *et al.* Long-term outcome of aortic dissection with patent false lumen: Predictive role of entry tear size and location. *Circulation* **125**, 3133–3141. https://doi.org/10.1161/CIRCULATIONAHA.111.090266 (2012).
14. Tolenaar, J. L. *et al.* Morphologic predictors of aortic dilatation in type B aortic dissection. *J. Vasc. Surg.* **58**, 1220–1225. https://doi.org/10.1016/J.JVS.2013.05.031 (2013).
15. Burris, N. S. *et al.* False lumen ejection fraction predicts growth in type B aortic dissection: Preliminary results. *Eur. J. Cardiothoracic Surg.* **57**, 896–903. https://doi.org/10.1093/ejcts/ezz343 (2020).
16. Marlevi, D. *et al.* False lumen pressure estimation in type B aortic dissection using 4D flow cardiovascular magnetic resonance: Comparisons with aortic growth. *J. Cardiovasc. Magn. Reson.* **23**, 51. https://doi.org/10.1186/S12968-021-00741-4 (2021).
17. Zadrazil, I., Corzo, C., Voulgaropoulos, V., Markides, C. N. & Xu, X. Y. A combined experimental and computational study of the flow characteristics in a Type B aortic dissection: Effect of primary and secondary tear size. *Chem. Eng. Res. Des.* **160**, 240–253. https://doi.org/10.1016/J.CHERD.2020.05.025 (2020).
18. Tse, K. M., Chiu, P., Lee, H. P. & Ho, P. Investigation of hemodynamics in the development of dissecting aneurysm within patient-specific dissecting aneurismal aortas using computational fluid dynamics (CFD) simulations. *J. Biomech.* **44**, 827–836. https://doi.org/10.1016/J.JBIOMECH.2010.12.014 (2011).
19. Cheng, Z., Wood, N. B., Gibbs, R. G. & Xu, X. Y. Geometric and flow features of type B aortic dissection: Initial findings and comparison of medically treated and stented cases. *Ann. Biomed. Eng.* **43**, 177–189. https://doi.org/10.1007/s10439-014-1075-8 (2014).
20. Xu, H. *et al.* Computed tomography-based hemodynamic index for aortic dissection. *J. Thorac. Cardiovasc. Surg.* **162**, e165–e176. https://doi.org/10.1016/J.JTCVS.2020.02.034 (2020).
21. Cuellar-Calabria, H. *et al.* Differences in the area of proximal and distal entry tears at CT angiography predict long-term clinical outcomes in aortic dissection. *Radiol. Cardiothorac. Imaging* **3**, e210029. https://doi.org/10.1148/RYCT.2021210029 (2021).
22. Fleischmann, D. & Burris, N. Entry tear dominance at CT angiography predicts long-term clinical outcomes in aortic dissection: Another piece of the puzzle. *Radiol. Cardithorac. Imaging* **3**, e210271. https://doi.org/10.1148/RYCT.2021210271 (2021).
23. Bäumler, K. *et al.* Fluid–structure interaction simulations of patient-specific aortic dissection. *Biomech. Model. Mechanobiol.* **19**, 1607–1628. https://doi.org/10.1007/s10237-020-01294-8 (2020).
24. Bäumler, K., Zimmermann, J., Ennis, D. B., Marsden, A. L. & Fleischmann, D. Hemodynamic effects of entry versus exit tear size and tissue stiffness in simulations of aortic dissection. *CMBBE Lect. Notes Comput. Vis. Biomech.* **38**, 143–152. https://doi.org/10.1007/978-3-031-10015-4_13 (2022).
25. Karmonik, C. *et al.* Computational study of haemodynamic effects of entry-and exit-tear coverage in a DeBakey type III aortic dissection: Technical report. *Eur. J. Vasc. Endovasc. Surg.* **42**, 172–177. https://doi.org/10.1016/j.ejvs.2011.04.008 (2011).
26. Shang, E. K. *et al.* Use of computational fluid dynamics studies in predicting aneurysmal degeneration of acute type B aortic dissections. *J. Vasc. Surg.* **62**, 279–284. https://doi.org/10.1016/j.jvs.2015.02.048 (2015).
27. Osswald, A. *et al.* Elevated wall shear stress in aortic type B dissection may relate to retrograde aortic type a dissection: A computational fluid dynamics pilot study. *Eur. J. Vasc. Endovasc. Surg.* **54**, 324–330. https://doi.org/10.1016/j.ejvs.2017.06.012 (2017).
28. Markl, M. *et al.* Time-resolved three-dimensional phase-contrast MRI. *J. Magn. Reson. Imaging* **17**, 499–506. https://doi.org/10.1002/jmri.10272 (2003).
29. de Beaufort, H. W. *et al.* Four-dimensional flow cardiovascular magnetic resonance in aortic dissection: Assessment in an ex vivo model and preliminary clinical experience. *J. Thorac. Cardiovasc. Surg.* **157**, 467–476. https://doi.org/10.1016/j.jtcvs.2018.06.022 (2019).
30. Dillon-Murphy, D., Noorani, A., Nordsletten, D. & Figueroa, C. A. Multi-modality image-based computational analysis of haemodynamics in aortic dissection. *Biomech. Model. Mechanobiol.* **15**, 857–76. https://doi.org/10.1007/s10237-015-0729-2 (2016).

31. Ruiz-Muñoz, A. *et al.* False lumen rotational flow and aortic stiffness are associated with aortic growth rate in patients with chronic aortic dissection of the descending aorta: A 4D flow cardiovascular magnetic resonance study. *J. Cardiovasc. Magn. Reson.* **24**, 20. https://doi.org/10.1186/S12968-022-00852-6 (2022).
32. Valvano, G. *et al.* Accelerating 4D flow MRI by exploiting low-rank matrix structure and hadamard sparsity. *Magn. Reson. Med.* **78**, 1330–1341. https://doi.org/10.1002/mrm.26508 (2017).
33. Ma, L. E. *et al.* Aortic 4D flow MRI in 2 minutes using compressed sensing, respiratory controlled adaptive k-space reordering, and inline reconstruction. *Magn. Reson. Med.* **81**, 3675–3690. https://doi.org/10.1002/mrm.27684 (2019).
34. Schnell, S. *et al.* K-t grappa accelerated four-dimensional flow MRI in the aorta: Effect on scan time, image quality, and quantification of flow and wall shear stress. *Magn. Reson. Med.* **72**, 522–533. https://doi.org/10.1002/mrm.24925 (2014).
35. Garg, P. *et al.* Comparison of fast acquisition strategies in whole-heart four-dimensional flow cardiac MR: Two-center, 1.5 tesla, phantom and *in vivo* validation study. *J. Magn. Reson. Imaging* **47**, 272–281. https://doi.org/10.1002/jmri.25746 (2018).
36. Loecher, M., Magrath, P., Aliotta, E. & Ennis, D. B. Time-optimized 4D phase contrast MRI with real-time convex optimization of gradient waveforms and fast excitation methods. *Magn. Reson. Med.* **82**, 213–2024. https://doi.org/10.1002/mrm.27716 (2019).
37. Dillinger, H., Walheim, J. & Kozerke, S. On the limitations of echo planar 4D flow MRI. *Magn. Reson. Med.* **84**, 1806–16. https://doi.org/10.1002/mrm.28236 (2020).
38. Pirola, S. *et al.* 4D flow MRI-based computational analysis of blood flow in patient-specific aortic dissection. *IEEE Trans. Biomed. Eng.* **66**, 3411–19. https://doi.org/10.1109/TBME.2019.2904885 (2019).
39. Zimmermann, J. *et al.* On the impact of vessel wall stiffness on quantitative flow dynamics in a synthetic model of the thoracic aorta. *Sci. Rep.* **11**, 6703. https://doi.org/10.1038/s41598-021-86174-6 (2021).
40. Lan, I. S. *et al.* Validation of the reduced unified continuum formulation against *in vitro* 4D-flow MRI. *Ann. Biomed. Eng.* **51**, 377–393. https://doi.org/10.1007/S10439-022-03038-4 (2023).
41. Updegrove, A. *et al.* Simvascular: An open source pipeline for cardiovascular simulation. *Ann. Biomed. Eng.* **45**, 525–541. https://doi.org/10.1007/s10439-016-1762-8 (2017).
42. Si, H. Adaptive tetrahedral mesh generation by constrained Delaunay refinement. *Int. J. Numer. Methods Eng.* **75**, 856–880. https://doi.org/10.1002/nme.2318 (2008).
43. Bazilevs, Y. *et al.* Computational vascular fluid–structure interaction: Methodology and application to cerebral aneurysms. *Biomech. Model. Mechanobiol.* **9**, 481–498. https://doi.org/10.1007/S10237-010-0189-7 (2010).
44. Moireau, P. *et al.* External tissue support and fluid–structure simulation in blood flows. *Biomech. Model. Mechanobiol.* **11**, 1–18. https://doi.org/10.1007/s10237-011-0289-z (2012).
45. Vignon-Clementel, I. E., Figueroa, C. A., Jansen, K. E. & Taylor, C. A. Outflow boundary conditions for three-dimensional finite element modeling of blood flow and pressure in arteries. *Comput. Methods Appl. Mech. Eng.* **195**, 3776–3796. https://doi.org/10.1016/J.CMA.2005.04.014 (2006).
46. Zhu, C. *et al.* svfsi: A multiphysics package for integrated cardiac modeling. *J. Open Source Softw.* **7**, 4118. https://doi.org/10.21105/JOSS.04118 (2022).
47. Marsden, A. L. & Esmaily-Moghadam, M. Multiscale modeling of cardiovascular flows for clinical decision support. *Appl. Mech. Rev.* **67**, 030804. https://doi.org/10.1115/1.4029909 (2015).
48. Esmaily-Moghadam, M., Bazilevs, Y. & Marsden, A. L. A bi-partitioned iterative algorithm for solving linear systems arising from incompressible flow problems. *Comput. Meth. Appl. Mech. Eng.* **286**, 40–62. https://doi.org/10.1016/j.cma.2014.11.033 (2015).
49. Esmaily-Moghadam, M., Bazilevs, Y., Hsia, T.-Y., Vignon-Clementel, I. E. & Marsden, A. L. A comparison of outlet boundary treatments for prevention of backflow divergence with relevance to blood flow simulations. *Comput. Mech.* **48**, 277–291. https://doi.org/10.1007/s00466-011-0599-0 (2011).
50. Tautz, L., Hennemuth, A. & Peitgen, H.-O. Motion analysis with quadrature filter based registration of tagged MRI sequences. *STACOM Lect. Notes Comput. Sci.* **7085**, 78–87. https://doi.org/10.1007/978-3-642-28326-0_8 (2012).
51. Markl, M. *et al.* Generalized reconstruction of phase contrast MRI: Analysis and correction of the effect of gradient field distortions. *Magn. Reson. Med.* **50**, 791–801. https://doi.org/10.1002/MRM.10582 (2003).
52. Meng, H., Tutino, V. M., Xiang, J. & Siddiqui, A. High WSS or low WSS? Complex interactions of hemodynamics with intracranial aneurysm initiation, growth, and rupture: Toward a unifying hypothesis. *Am. J. Neurorad.* **35**, 1254–1262. https://doi.org/10.3174/ajnr.A3558 (2014).
53. Wang, H., Uhlmann, K., Vedula, V., Balzani, D. & Varnik, F. Fluid–structure interaction simulation of tissue degradation and its effects on intra-aneurysm hemodynamics. *Biomech. Model. Mechanobiol.* **21**, 671–683. https://doi.org/10.1007/S10237-022-01556-7 (2022).
54. Riesenkampff, E. *et al.* Pressure fields by flow-sensitive, 4d, velocity-encoded CMR in patients with aortic coarctation. *JACC Cardiovasc. Imaging* **7**, 920–926. https://doi.org/10.1016/j.jcmg.2014.03.017 (2014).
55. Urbina, J. *et al.* Realistic aortic phantom to study hemodynamics using MRI and cardiac catheterization in normal and aortic coarctation conditions. *J. Magn. Reson. Imaging* **44**, 683–697. https://doi.org/10.1002/jmri.25208 (2016).
56. Al-Azawy, M. G., Turan, A. & Revell, A. Investigating the impact of non-Newtonian blood models within a heart pump. *Int. J. Numer. Meth. Biomed. Eng.* **33**, e02780. https://doi.org/10.1002/cnm.2780 (2017).
57. Liu, H. *et al.* Comparison of Newtonian and non-Newtonian fluid models in blood flow simulation in patients with intracranial arterial stenosis. *Front. Physiol.* **12**, 718540. https://doi.org/10.3389/fphys.2021.718540 (2021).

Acknowledgements

We thank Shannon Walters, Chris LeCastillo, and Kyle Gifford (Stanford 3DQ Lab) for their 3D printing support and services, and Nicole Schiavone (Stanford Mechanical Engineering) for advice about the technical setup. We acknowledge the computational infrastructure (Sherlock HPC cluster) provided by the Stanford Research Computing Center. Funding was received through DAAD doctoral candidate scholarship (to J.Z.), NIH R01 LM013120 (to A.L.M.) and NIH R01 HL131823 (to D.B.E.).

Author contributions

J.Z. and K.B. jointly conceptualized the study, performed cross-modality data analysis, prepared figures, and wrote the manuscript. J.Z. engineered the flow loop setup and led experimental MRI studies. K.B. developed the computational simulations framework and performed FSI simulations. M.L. and T.E.C. supported experimental data acquisition and reconstruction. A.L.M. conceptualized the study and supervised computational simulation work. D.B.E. conceptualized the study and supervised experimental data acquisition. D.F. conceptualized the study and provided overall advice to the research objective. All authors critically revised and approved the manuscript.

Competing interests
ALM is an editorial board member of the journal and serves as guest editor of this special issue.

Additional information
Supplementary Information The online version contains supplementary material available at https://doi.org/10.1038/s41598-023-49942-0.

Correspondence and requests for materials should be addressed to K.B.

Reprints and permissions information is available at www.nature.com/reprints.

Publisher's note Springer Nature remains neutral with regard to jurisdictional claims in published maps and institutional affiliations.